AMSI SUMMERRESEARCH SCHOLARSHIPS 2023–24

SET YOUR SIGHTS ON RESEARCH THIS SUMMER

The Coriolis Force acting on Magnetic Active Regions on the Sun

Liam Barnes

Supervised by Dr. Hannah Schunker

University of Newcastle

AMSI AUSTRALIAN MATHEMATICAL SCIENCES INSTITUTE

1 Abstract

The Sun is a magnetic star, generating a magnetic activity cycle with an 11-year period. At the end of each cycle, the Sun's large scale poloidal magnetic field reverses its polarity. Throughout a solar cycle, magnetically active regions form on the Sun's surface, characterised by areas of strong magnetic fields with a bipole structure. Joy's Law is an empirical observation where these active region bipoles tend to be tilted away from east-west alignment, with the polarity in the prograde direction closer to the equator. In some models of the solar dynamo, Joy's Law is important in reversing the global poloidal magnetic field from one cycle to the next. It is thought that Joy's Law is driven by the Coriolis force from the Sun's rotation because the active region tilt angle increases with latitude in a similar way to the Coriolis force. However, it is not fully understood what plasma flows the Coriolis force acts on to produce this tilt. Our aim is to determine if Joy's Law is due to flows associated with the magnetic field, or passively driven by surrounding plasma flows. We calculated the force terms in the equation of motion for three-dimensional magnetohydrodynamic simulations, including the Coriolis force, of a submerged magnetic flux tube rising through convection in the near-surface of the Sun. We found that the tilt induced by the Coriolis force causes a minor increase in the magnetic tension and magnetic pressure forces. This suggests that Joy's Law is a passive effect, which suggests that the tilt behaviour is driven by the surrounding plasma flows.

2 Introduction

The Sun is a magnetic main-sequence star, with an 11-year activity cycle, and rotates with an average period of 27 days. Throughout an activity cycle, magnetic active regions, characterised by areas with strong magnetic field with a bipole structure, form on the Sun's surface. At the end of each solar activity cycle, the Sun's large scale poloidal magnetic field reverses its polarity, which also reverses the polarity of the active region bipoles that form.

2.1 Magnetic Active Regions

Active regions on the surface of the Sun are characterised by areas of strong magnetic flux, typically 100 Mm in size with magnetic field strength on the order of 100 G [3]. Active regions are believed to be caused by coherent magnetic flux tubes deep below the surface, which rise due to magnetic buoyancy. This forms an Ω-shaped loop and breaks through the photosphere (the Sun's surface layer), as illustrated in Figure 1a. In this model, a magnetic bipole structure can be seen, with upward and downward magnetic flux through the photosphere on each side of the loop.

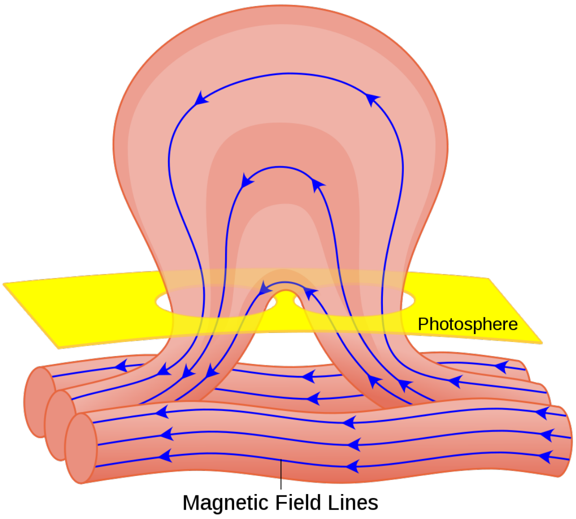

(a)

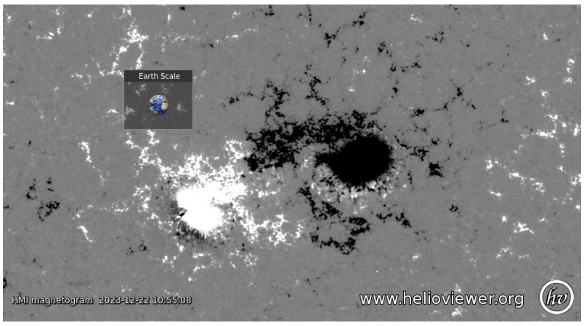

(b)

Figure 1: Left panel: Cartoon model of a submerged magnetic flux tube piercing the surface of the Sun producing an opposite polarity pair at the surface [8]. Right panel: Observations of the line-of-sight magnetic field of an active region from NASA's Solar Dynamics Observatory Helioseismic and Magnetic Imager (SDO/HMI) [2].

This bipole structure can be seen in magnetogram images of the Sun, which show the line-of-sight magnetic field with white corresponding to flux coming out of the surface and black corresponding to flux going into the surface. Figure 1b shows the line-of-sight magnetic field of an active region with a clear bipole. These concentrated areas of magnetic flux form *sunspots*, which are dark, relatively cool spots on the Sun's surface. Not all active regions produce fully formed, long-lived sunspots with a central umbra (dark region) and surrounding penumbra, but all active regions cause enough cooling to produce a darkening on the surface.

2.2 Joy's Law

Joy's law is a statistical law, asserting that sunspot pairs have a preferential tilt towards the equator, away from east-west alignment. More precisely, the leading sunspot (with respect to the Sun's rotation) in an active region bipole is closer to the equator than the following spot (see Figure 2).

Observational analysis has shown that the tilt described by Joy's Law acts after the active region has emerged through the surface [4], in contradiction to traditional thin-flux tube theory where the tilt is formed below the surface as the flux tube rises [6, 7].

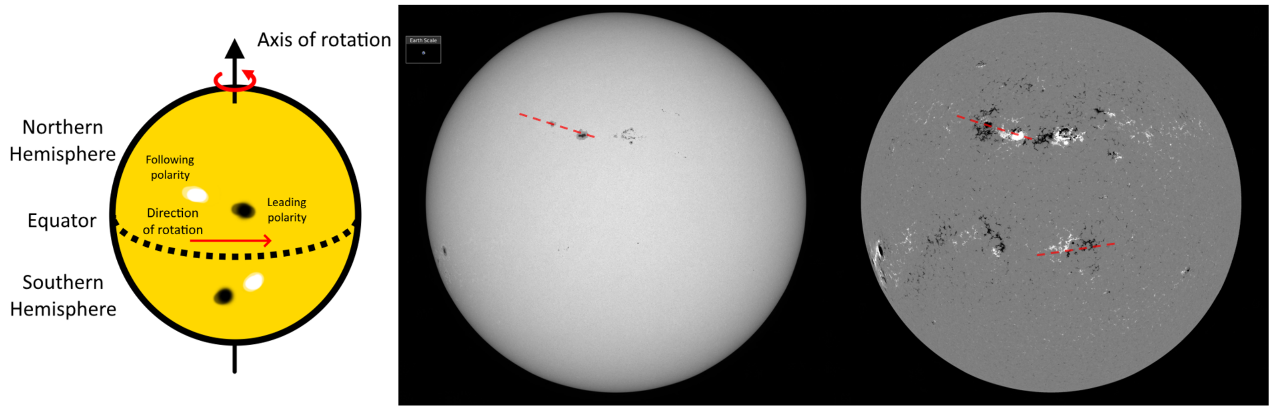

Figure 2: Left panel: Cartoon illustration of Joy's Law. Right Panel: observed intensity continuum of the Sun showing sunspots, and the corresponding line-of-sight magnetic field observation from SDO/HMI [2]. The concentrated regions of magnetic field that form sunspots within active regions are clear. The red dashed lines indicate the rough axis connecting the bipoles of the active region which indicates the tilt angle.

The tilt angle of active regions is observed to increase with the latitude of the active region [1]. [4] showed that this latitudinal dependency is only in the north-south separation of the bipoles, and not the east-west. This suggests that Joy's Law is driven by the Coriolis Force acting on some east-west plasma flows as the active region grows in size and the bipoles separate.

After approximately two days, the active region emergence process ends and it remains at the fixed tilt angle [4]. The aim of this project is to determine what effect the Coriolis force has on the force terms in the magnetohydrodynamic equation of motion (see section 3.2), by analysing numerical simulations of the emergence process. In the following report, I describe my analysis of the three-dimensional active region simulations, the methods I implemented to compute the relevant force terms from the simulated data, and key findings from the comparisons of the different force terms.

2.3 Statement of Authorship

Data from the MURaM code [5] simulations were produced by William-Roland Batty. All analysis was performed by the author, Liam Barnes, under the guidance of Dr. Hannah Schunker and William Roland-Batty. All force term expansions, derivations, analysis code, figures and results are solely the work of the author.

3 Background

3.1 The Coriolis Force

At a point on the surface of the Sun, we define a cartesian coordinate system (x, y, z), with East being the positive x-direction, North being the positive y-direction, and z is in the outward radial direction from the Sun's centre. This coordinate axis is fixed at a particular point on the surface as the Sun rotates, and is thus a rotating frame of reference.

The Coriolis Force is a pseudo force experienced by objects moving in a rotating frame of reference. It is given by:

$$\begin{gathered}\mathbf{a_c} = 2\boldsymbol{\Omega} \times \mathbf{v} = \langle 2v_z\Omega\cos\theta - 2v_y\Omega\sin\theta, 2v_x\Omega\sin\theta, -2v_x\Omega\cos\theta\rangle \\ \mathbf{F_c} = \rho\mathbf{a_c}\end{gathered} \tag{1}$$

where $\mathbf{F_c}$ is the Coriolis Force, $\boldsymbol{\Omega}$ is the angular rotation of the frame of reference (in our case the Sun's angular rotation rate $\boldsymbol{\Omega}_\odot$), θ is the latitude of the area of interest, and $\mathbf{v} = (v_x, v_y, v_z)$ is the velocity of the object within the rotating frame of reference.

If we assume that the contribution of the vertical component (v_z) of plasma velocity to the Coriolis force is negligible, and also neglect the vertical effect of the Coriolis force, we have the *f-plane approximation*:

$$2\Omega \times \mathbf{v} \approx \langle -fv_y, fv_x, 0\rangle \tag{2}$$

where $f = 2\Omega \sin\theta$, which increases in magnitude as the latitude θ increases in magnitude ($-\frac{\pi}{2} < \theta < \frac{\pi}{2}$). Areas of strong magnetic field suppress vertical plasma convection (v_z), so the f-plane approximation is valid in our case.

3.2 Magnetohydrodynamics

3.2.1 Fundamental Equations

Magnetohydrodynamics (MHD) is the study of the dynamics of electrically conductive fluids, such as the plasma near the surface of the Sun. Combining the equations of fluid dynamics and electromagnetism yields the fundamental equations of MHD:

$$\frac{\partial \mathbf{B}}{\partial t} = \nabla \times (\mathbf{v} \times \mathbf{B}) + \eta \nabla^2 \mathbf{B} \tag{3}$$

$$\frac{\partial \rho}{\partial t} + \nabla \cdot (\rho \mathbf{v}) = 0 \tag{4}$$

$$\rho \frac{d\mathbf{v}}{dt} = -\nabla p + \mathbf{j} \times \mathbf{B} + \rho\nu \left[\nabla^2 \mathbf{v} + \frac{1}{3} \nabla (\nabla \cdot \mathbf{v}) \right] + \mathbf{F_g} \tag{5}$$

$$p = \frac{k_B}{m} \rho T \tag{6}$$

$$\frac{\rho^\gamma}{\gamma - 1} \frac{d}{dt} \left(\frac{p}{\rho^\gamma} \right) = -\nabla \cdot \mathbf{q} - L_r + {}^{j^2}\!/_{\sigma} + F_H \tag{7}$$

Eqn. (3) is the induction equation, with $\mathbf{B} = \langle B_x, B_y, B_z \rangle$ the magnetic field strength vector, $\mathbf{v} = \langle v_x, v_y, v_z \rangle$ the plasma velocity and $\eta = \frac{1}{\sigma\mu}$ the magnetic diffusivity with σ the conductivity and μ the magnetic permeability.

Eqn. (4) is the continuity equation, with ρ the plasma density.

Eqn. (5) is the equation of motion, with $\mathbf{j}$ the current density, ν the kinematic plasma viscosity and p the plasma pressure.

Eqn. (6) is the ideal gas law, with k_B the Boltzmann constant, m the mean particle mass and T the temperature.

Eqn. (7) is the energy equation, with γ the adiabatic exponent, $\mathbf{q}$ the heat flux due to particle conduction, L_r the net radiation and F_H represents all other heating sources.

3.2.2 Ideal MHD

From the induction equation (Eqn. (3)), we can define the *magnetic Reynold's number* $R_m = \frac{l_0 V_0}{\eta}$, which represents the ratio of the first term on the right (convective term) to the second term on the right (diffusive term) in (3).

In the ideal limit (ideal MHD), $R_m >> 1$, and the diffusive term in (3) can be neglected. In this case, it can be shown that the magnetic field is frozen to the plasma (the magnetic field moves with the plasma) by Alfvén's Frozen Flux Theorem [3]. At the Sun's surface, R_m is in fact large, and ideal MHD applies.

3.2.3 Equation of Motion and The Lorentz Force

Of particular interest in this project is the equation of motion (Eqn. (5)), which describes how the plasma moves in response to the various forces. The right hand side of Eqn. (5) contains the pressure gradient (∇p), the Lorentz force ($\mathbf{j} \times \mathbf{B}$), viscous stress ($\rho\nu \left[\nabla^2 \mathbf{v} + \frac{1}{3}\nabla(\nabla \cdot \mathbf{v})\right]$), and the gravity force ($\mathbf{F_g}$).

The current density $\mathbf{j}$ can be eliminated from the Lorentz force using Ampère's Law $\mathbf{j} = \nabla \times \mathbf{B}/\mu$ and a vector identity, giving:

$$\mathbf{j} \times \mathbf{B} = \frac{(\mathbf{B} \cdot \nabla)\mathbf{B}}{\mu} - \nabla \left(\frac{B^2}{2\mu} \right) \tag{8}$$

The first term on the right hand side of (Eqn. 8) is the magnetic tension force, and the second term is the magnetic pressure gradient.

The magnetic tension force arises when the magnetic field lines are curved, and acts inwards towards the centre of curvature to try and straighten the field lines. The magnetic pressure gradient arises when the magnetic field strength (spacing of the field lines) is non-uniform, and acts in the direction from how to low flux concentration.

The magnetic tension, magnetic pressure gradient and viscous stress are the main forces of interest in this project.

4 MURaM Simulations

The Max-Planck-Institute for Aeronomy/University of Chicago Radiation Magneto-hydrodynamics code (MURaM) is a numerical code that solves the MHD equations in a three-dimensional cartesian domain near the surface of the Sun (as outlined in section 3.1) [5].

4.1 Simulation Domain and Initial Conditions

The particular simulations for this project use a domain that is 96 Mm $\times$ 96 Mm horizontally (x, y) and 16 Mm vertically in depth (z), with the surface layer positioned 1 Mm below the top of the domain. The initial conditions contain a magnetic flux tube artificially inserted approximately 11 Mm below the surface into a background of self-consistently simulated convection. It is aligned parallel to the x-axis and has a Gaussian strength profile with peak strength of 5×10^4 G, with a full-width at half-maximum of 1.33 Mm and is set to zero at a radius of 1.7 Mm. As the simulation runs, the flux tube rises due to imposed magnetic buoyancy, ultimately emerging through the surface as an Ω-shaped loop and a bipole structure at the surface.

We analyse the output of two simulations, both with the identical initial conditions described above, however one accounts for the Sun's rotation. It does this by including the Coriolis force (with the f-plane approximation, (Eqn. (2))) in the equation of motion (Eqn. (5)), which becomes:

$$\rho \frac{d\mathbf{v}}{dt} = -\nabla p + \mathbf{j} \times \mathbf{B} + \rho\nu \left[\nabla^2 \mathbf{v} + \frac{1}{3}\nabla(\nabla \cdot \mathbf{v} \right] + \mathbf{F_g} - \mathbf{F_c} \tag{9}$$

The second simulation uses an angular rotation $\Omega = 100\Omega_\odot$, i.e 100 times that of the Sun's true rotation speed, $\Omega_\odot$, in order to generate a measureable effect in the limited simulation time as the flux emerges (≈ 16 solar hours).

4.2 Physical Quantities

The simulations covers a volume of 96 Mm $\times$ 96 Mm $\times$ 16 Mm discretised onto a grid of $1008 \times 1008 \times 504$ points. At each grid point, and for all 301 timesteps, the simulation outputs all primary variables required for further analysis. The variables of interest are the three components of the magnetic field (B_x, B_y, B_z), the three components of plasma velocity (v_x, v_y, v_z), pressure (p), and density (ρ). All quantities are given in centimetre-gram-second (CGS) units, with magnetic field given in Gauss (G), velocity in cm/s, density in g/cm^3 and pressure in dyn/cm^2, $(1dyn = 10^{-5}N)$. For this project, we only analysed the surface slice, so the domain

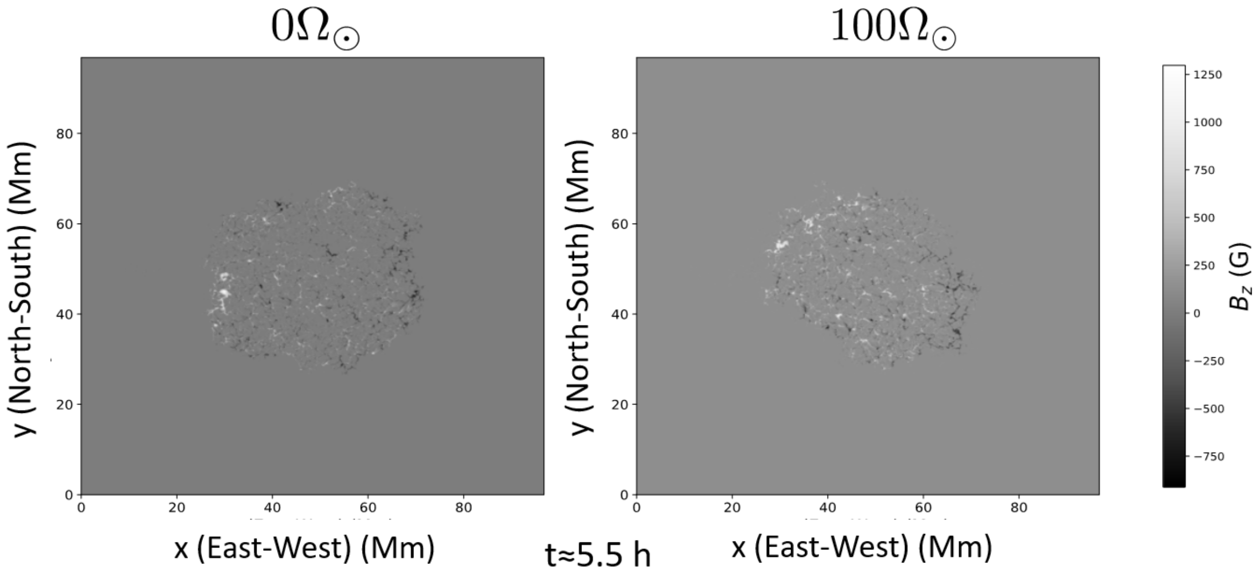

Figure 3: Vertical magnetic field component at the surface of the simulation without rotation (left) and with one hundred times solar rotation (right) 5.5 hrs after the beginning of the simulation.

of interest is a 1008×1008 horizontal grid with 301 timesteps (corresponding to approximately 16 hours). This domain can be seen in Figure 3.

5 Computing Force Terms

Writing $\mathbf{B} = (B_x, B_y, B_z)$ and $\mathbf{v} = (v_x, v_y, v_z)$, the magnetic tension, magnetic pressure and viscous stress force terms can be expanded into a form suitable for numerical computation. We have magnetic tension:

$$\mathbf{T} = \frac{(\mathbf{B}\cdot\nabla)\mathbf{B}}{\mu} = \frac{1}{\mu}\begin{bmatrix} B_x\frac{\partial B_x}{\partial x} + B_y\frac{\partial B_x}{\partial y} + B_z\frac{\partial B_x}{\partial z} \\ B_x\frac{\partial B_y}{\partial x} + B_y\frac{\partial B_y}{\partial y} + B_z\frac{\partial B_y}{\partial z} \\ B_x\frac{\partial B_z}{\partial x} + B_y\frac{\partial B_z}{\partial y} + B_z\frac{\partial B_z}{\partial z} \end{bmatrix} = \begin{bmatrix} T_x \\ T_y \\ T_z \end{bmatrix} \tag{10}$$

magnetic pressure

$$\mathbf{P_m} = \nabla\left(\frac{B^2}{2\mu}\right) = \frac{1}{\mu}\begin{bmatrix} B_x\frac{\partial B_x}{\partial x} + B_y\frac{\partial B_y}{\partial x} + B_z\frac{\partial B_z}{\partial x} \\ B_x\frac{\partial B_x}{\partial y} + B_y\frac{\partial B_y}{\partial y} + B_z\frac{\partial B_z}{\partial y} \\ B_x\frac{\partial B_x}{\partial z} + B_y\frac{\partial B_y}{\partial z} + B_z\frac{\partial B_z}{\partial z} \end{bmatrix} = \begin{bmatrix} P_{m_x} \\ P_{m_y} \\ P_{m_z} \end{bmatrix} \tag{11}$$

and from the viscous stress term $\rho\nu\left[\nabla^2\mathbf{v}+\frac{1}{3}\nabla(\nabla\cdot\mathbf{v})\right]$ we have

$$\begin{aligned}\nabla^2\mathbf{v} &= \begin{bmatrix}\frac{\partial^2 v_x}{\partial x^2}+\frac{\partial^2 v_x}{\partial y^2}+\frac{\partial^2 v_x}{\partial z^2}\\ \frac{\partial^2 v_y}{\partial x^2}+\frac{\partial^2 v_y}{\partial y^2}+\frac{\partial^2 v_y}{\partial z^2}\\ \frac{\partial^2 v_z}{\partial x^2}+\frac{\partial^2 v_z}{\partial y^2}+\frac{\partial^2 v_z}{\partial z^2}\end{bmatrix}\\ \nabla(\nabla\cdot\mathbf{v}) &= \begin{bmatrix}\frac{\partial^2 v_x}{\partial x^2}+\frac{\partial^2 v_y}{\partial x\partial y}+\frac{\partial^2 v_z}{\partial x\partial z}\\ \frac{\partial^2 v_x}{\partial x\partial y}+\frac{\partial^2 v_y}{\partial y^2}+\frac{\partial^2 v_z}{\partial y\partial z}\\ \frac{\partial^2 v_x}{\partial x\partial z}+\frac{\partial^2 v_y}{\partial y\partial z}+\frac{\partial^2 v_z}{\partial z^2}\end{bmatrix}\end{aligned} \tag{12}$$

To compute the required spatial derivatives, the following fourth-order centred difference approximations were used:

$$f'(x)=\frac{-f(x+2\Delta x)+8f(x+\Delta x)-8f(x-\Delta x)+f(x-2\Delta x)}{12\Delta x}+O(\Delta x^4) \tag{13}$$

$$f''(x)=\frac{-f(x+2\Delta x)+16f(x+\Delta x)-30f(x)+16f(x-\Delta x)-f(x-2\Delta x)}{12\Delta x^2}+O(\Delta x^4) \tag{14}$$

The data from the simulations was loaded into `Python` as numpy arrays, with a $1008\times 1008\times 301$ array for each quantity of interest, which are listed in section 4.2. The difference formulas (13) and (14) were applied to these arrays, creating new arrays of the same dimension for each derivative of each quantity. (For example, $\frac{\partial B_x}{\partial y}$ is defined at all 1008×1008 grid points, for all 301 timesteps.) These derivative arrays were then used to compute the three components of each force, as shown in Eqns. (10), (11) and (12).

With each force now stored in their own arrays, analysis of the difference force terms in each simulation were possible. Shown in Figure 4 is the total magnitude of magnetic tension ($|\mathbf{T}|=({T_x}^2+{T_y}^2+{T_z}^2)^{\frac{1}{2}}$), computed from the T_x, T_y and T_z arrays.

6 Comparing Force Terms

6.1 Masking

It only makes sense to compute the force terms where there is a significant magnetic field strength. Thus, when comparing the force terms, we first applied a mask to the force arrays. This mask selects the grid points at each time slice where the vertical component of magnetic

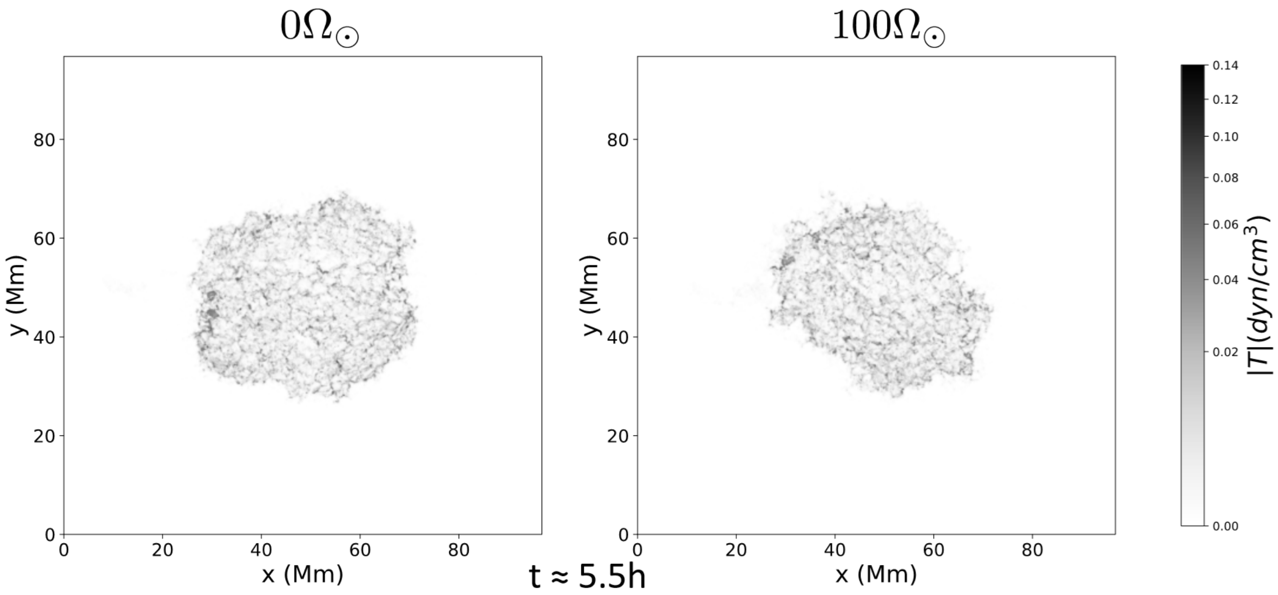

Figure 4: Magnitude of the magnetic tension at the surface of the simulation without rotation (left) and with one hundred times solar rotation (right) 5.5 hrs after the beginning of the simulation.

field is significant. For this project, the mask selects grid points where $|B_z| > 100G$. This mask, at a particular time step for the simulation that includes the Coriolis force, is illustrated in Figure 5

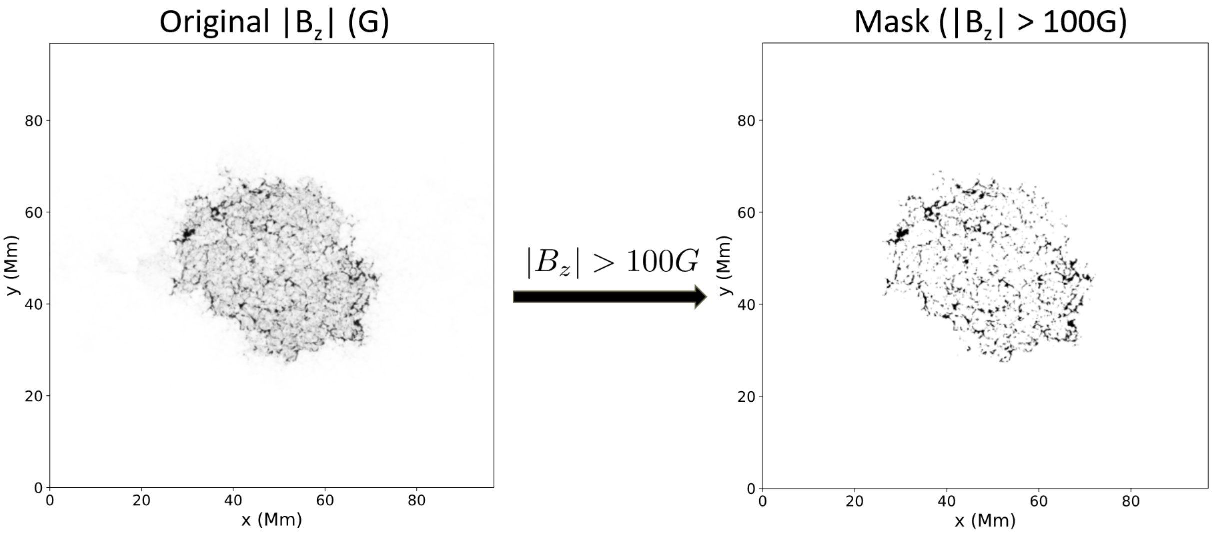

Figure 5: Unsigned vertical magnetic field strength, $|B_z|$, at the surface of the simulation with one hundred times solar rotation 5.5 hrs after the beginning of the simulation (left) and the right shows where $|B_z| > 100$ G.

6.2 Masked Averages

The force terms in both simulations can now be meaningfully compared within the region of interest using the masking method in Section 6.1. At each time step, a mask was generated and applied to each array at the same time step. With this mask applied, the average of the magnitude of each force was taken and stored in an array. For each force, this generated an array with 301 entries, each entry corresponding to the masked average of that force at a particular time step. This was done for both simulations.

Taking the average over these arrays results in a total average magnitude value of each force, giving a rudimentary summary of the relative sizes of each force term. These total averages are presented in Figure 6. The error bars represent the temporal standard deviation, indicating how the average over the mask for each force varies with time.

Figure 6 shows a difference in the magnetic tension and pressure forces between the two simulations. It is worth noting that both of these forces are proportional to B^2. Thus, it is natural to ask whether this difference is directly attributable to the introduction of the Coriolis force, or if a difference in the total magnetic field strength between the simulations is causing this discrepancy. Figure 7a shows the spatial averages of B^2 over time for each simulation.

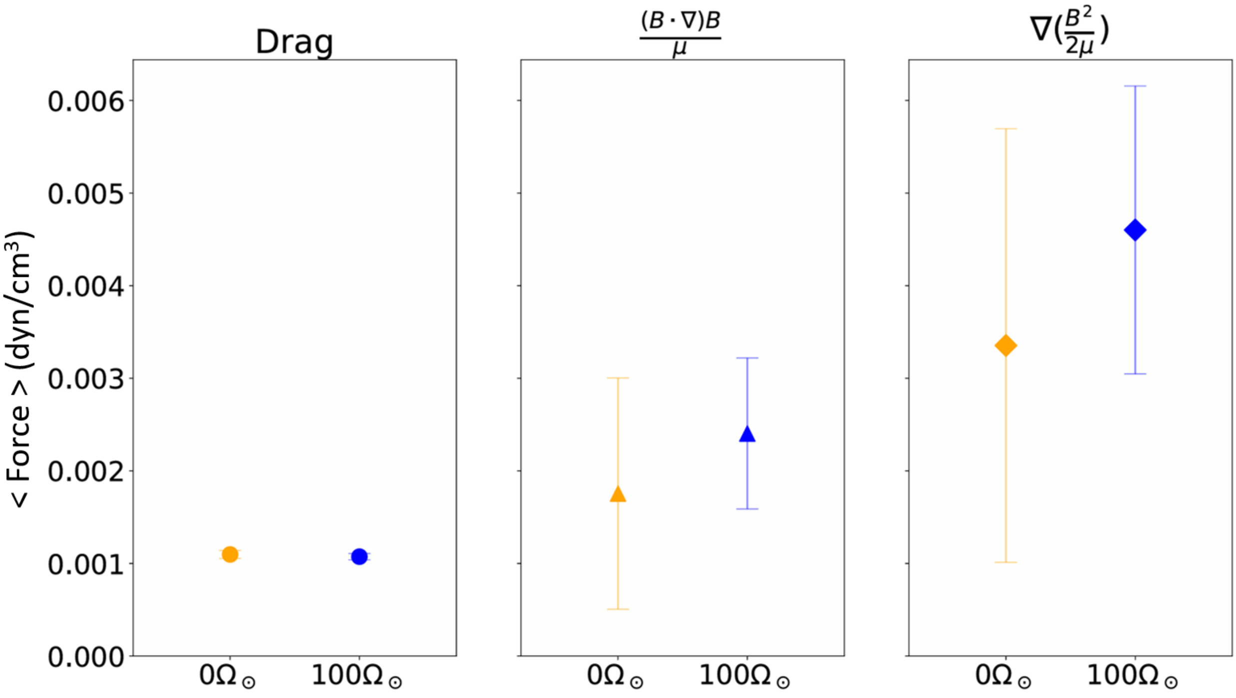

Figure 6: Mean of the force terms where $|B_z| > 100$ G from $t = 5.5$ hrs until $t_{\text{end}} = 16$ hrs for both simulations without rotation and with one hundred times solar rotation. The uncertainties are the standard deviation of the mean over time. The simulation with rotation produces marginally larger magnetic tension and magnetic pressure terms.

The magnetic tension and pressure force averages were then normalised by the total average of B^2 for each simulation in an attempt to eliminate the influence of the differing magnetic field strength profiles between the two simulations. These normalised averages are shown in Figure 7b.

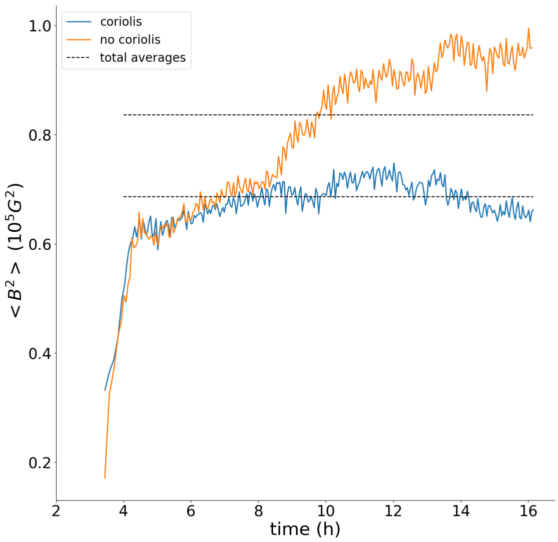

(a)

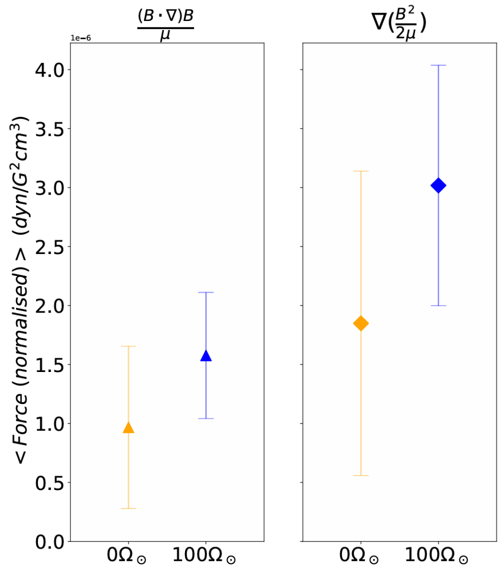

(b)

Figure 7: Left panel: Spatial average of B^2 over time. Less flux emerges at the surface for the simulation including rotation. Right panel: Magnetic tension and magnetic pressure normalised by the mean of B^2 over time and space, indicated by the dashed lines in the left panel, in order to compare the simulations.

7 Discussion and Conclusion

From Figure 6, the viscous stress (drag) force is the least significant. This is likely attributable to the fact that plasma convection is inhibited by the strong magnetic field, and viscous stress is proportional to velocity, so this is perhaps not surprising.

Magnetic tension and, in particular, magnetic pressure appear much more significant than viscous stress at the bipole, and this is true for both simulations. Furthermore, both forces are larger in magnitude for the simulation with the Coriolis force. This suggests that the tilt induced by the Coriolis force has increased the magnetic tension and pressure forces. However, this difference is not very significant, and the forces in the two simulations are well within temporal standard deviations of each other, as shown by the error bars in Figure 6.

Upon normalising by B^2 (Figure 7b), the difference is actually slightly more significant, further implying that the Coriolis force is having a direct effect on the magnetic tension and pressure forces. The difference is still not hugely significant, and the normalised forces still remain within temporal standard deviations of each other.

The difference in the magnetic forces between the two simulations does not appear sufficient to play a major role in the bipole's observed motion, or lack thereof, in the presence of the Coriolis force. Additionally, the low amount of viscous stress within the bipole, and the limited plasma convection, suggests that the Coriolis force is also not acting strongly within the bipole, as the Coriolis Force is proportional to plasma velocity.

These observations suggest that Joy's law is a passive phenomenon, with the Coriolis force acting on the plasma flows surrounding the coherent magnetic bipoles. Including rotational effects in the simulation increases the magnetic tension and pressure forces a small amount, but not significantly enough to conclude that the mechanism behind Joy's Law is magnetically dominated.

These conclusions relate only to the surface slice of the simulations. Further analysis should be conducted below the surface slice as the magnetic bipole emerges. Perhaps the Coriolis force, as well as the magnetic tension, magnetic pressure and viscous stress forces, are playing a larger role beneath the surface.

The different components (x and y) of each force should also be examined separately, as this may provide more insight into the mechanism that causes the bipoles to settle at a fixed tilt.

It is also worth noting that this project focus on simulations with a single, specific initial state of convection. Running more simulations with different initial conditions of plasma flows may provide more insight into the general properties of active regions, and perhaps a more coherent bipole will form in a different pattern of convection. As with all science, the more data we have, the more confident we can be in the conclusions we draw from it.

Acknowledgements

I would like to acknowledge the incredible support and guidance provided by my supervisor, Dr. Hannah Schunker, throughout the duration of this project, and for the invaluable learning experience it has provided. I would also like to thank William Roland-Batty for all of his help and guidance, and acknowledge that this project utilises ideas and simulations produced by William as part of his research.

References

[1] G. E. Hale, F. Ellerman, S. B. Nicholson, and A. H. Joy. The Magnetic Polarity of Sun-Spots. , 49:153, April 1919. https://doi.org/10.1086/142452 `doi:10.1086/142452`.

[2] W. Dean Pesnell, B. J. Thompson, and P. C. Chamberlin. The Solar Dynamics Observatory (SDO). , 275(1-2):3–15, January 2012. https://doi.org/10.1007/s11207-011-9841-3 `doi:10.1007/s11207-011-9841-3`.

[3] Eric Priest. *Magnetohydrodynamics of the Sun*. Cambridge University Press, 2014.

[4] H. Schunker, C. Baumgartner, A. C. Birch, R. H. Cameron, D. C. Braun, and L. Gizon. Average motion of emerging solar active region polarities. II. Joy's law. , 640:A116, August 2020. http://arxiv.org/abs/2006.05565 `arXiv:2006.05565`, https://doi.org/10.1051/0004-6361/201937322 `doi:10.1051/0004-6361/201937322`.

[5] A. Vögler, S. Shelyag, M. Schüssler, F. Cattaneo, T. Emonet, and T. Linde. Simulations of magneto-convection in the solar photosphere. Equations, methods, and results of the MURaM code. , 429:335–351, January 2005. https://doi.org/10.1051/0004-6361:20041507 `doi:10.1051/0004-6361:20041507`.

[6] Maria A. Weber, Yuhong Fan, and Mark S. Miesch. The Rise of Active Region Flux Tubes in the Turbulent Solar Convective Envelope. , 741(1):11, November 2011. http://arxiv.org/abs/1109.0240 `arXiv:1109.0240`, https://doi.org/10.1088/0004-637X/741/1/11 `doi:10.1088/0004-637X/741/1/11`.

[7] Maria A. Weber, Hannah Schunker, Laurène Jouve, and Emre Işık. Understanding active region origins and emergence on the sun and other cool stars. *Space Science Reviews*, 219(8):63, 2023. https://doi.org/10.1007/s11214-023-01006-5 `doi:10.1007/s11214-023-01006-5`.

[8] Wikipedia contributors. Active region — Wikipedia, the free encyclopedia, 2023. URL: `https://en.wikipedia.org/w/index.php?title=Active_region&oldid=1189299533`.